10.1002/anie.202414479

WILEY VCH

RESEARCH ARTICLE

Dual Ion Co-insertion Induced Spontaneous and Reversible Phase Conversion Chemistry for Unprecedented Zn^{2+} Storage

Xikun Zhang[a,b], Junwei Zhang[a], Haoxiang Yu[a], Thomas L. Madanu[b], Maoting Xia[a], Pengcheng Xing[b], Alexandru Vlad[c], Jie Shu*[a], and Bao-Lian Su*[b,d,e]

[a] X.K. Zhang, J.W. Zhang, Dr. H.X. Yu, M.T. Xia, Prof. J. Shu
School of Materials Science and Chemical Engineering
Ningbo University
818 Fenghua road, Ningbo, Zhejiang, 315211, China
E-mail: shujie@nbu.edu.cn

[b] X.K. Zhang, Dr. T.L. Madanu, Dr. P.C. Xing, Prof. B.-L. Su
Laboratory of Inorganic Materials Chemistry (CMI)
University of Namur
61 rue de Bruxelles, Namur, B-5000, Belgium
E-mail: bao-lian.su@unamur.be (B.-L. Su)

[c] Prof. A. Vlad
Institute of Condensed Matter and Nanosciences, Molecular Chemistry, Materials and Catalysis
Université Catholique de Louvain
Louvain-la-Neuve, B-1348, Belgium

[d] Prof. B.-L. Su
State Key Laboratory of Advanced Technology for Materials Synthesis and Processing
Wuhan University of Technology
122 Luoshi road, Wuhan, Hubei, 430070, China
E-mail: bao-lian.su@unamur.be (B.-L. Su)

[e] Prof. B.-L. Su
Clare Hall
University of Cambridge
Cambridge, CB2 1EW, UK
E-mail: bao-lian.su@unamur.be (B.-L. Su)

Abstract: Prussian blue analogues are highly promising electrode materials due to their versatile electrochemical activity and low cost. However, they often suffer from severe structural damage caused by the Jahn-Teller distortion and dissolution of high-spin outer metal ions, resulting in poor cycle life. Material modification and electrolyte regulation have been the common approaches to address this issue, albeit with very limited success. We report here a novel and efficient strategy to preserve structural stability by co-inserting Co^{2+} and Zn^{2+} ions in $KCo[Fe(CN)_6]$. This co-insertion induced a spontaneous and reversible phase conversion by the replacement of low-spin inner ion (Fe^{3+}), which efficiently relieves structural damage caused by Jahn-Teller distortion and metal-ion dissolution, leading to an outstanding Zn^{2+} storage capacity and an exceptional improvement of cycle life with a capacity retention of 97.7% over 4400 cycles at 40 C. We also demonstrated the enhancement of co-intercalation on ion migration using a combined approach of experimental and density functional theory (DFT) calculations. This work provides an important progress to solve the cycle stability of Prussian blue analogues towards their practical application as electrode materials for aqueous batteries.

Introduction

Prussian blue analogues (PBAs) have been widely used in aqueous energy storage systems owing to their open skeleton to store charge carriers like monovalent,[1-4] multivalent[5-7] and non-metal ions[8-10] and the ease of synthesis. PBAs are typically inorganic coordination compounds formed by transition metal ions connected through cyanide bridges (-CN-). They are generally composed of high-spin outer transition metal ion and inner group, which consists of low-spin inner transition metal ion and -CN- group. Their open framework structures and two-electron reaction centers enable them to possess high theoretical capacity with a good volume change tolerance.[11-15] However, most of PBAs suffer from serious structural damage during repeated ion insertion/extraction in aqueous electrolyte, resulting in drastic capacity decay.[16-19] This is primarily due to the precipitation of high-spin outer ions of the PBAs crystal lattice via their dissolution during cycling,[11,20,21] leading to the pulverization, even shedding of host materials. Secondly, especially in some Mn- and Ni-based PBAs, the inevitable Jahn-Teller distortion of the geometric configuration of the framework can also lead to structural deformation, being detrimental to ion transport and structural stability.[6,11,20] As a result, some PBAs manifests poor cycling performance.[22,23]

Various methods like material modification and electrolyte regulation have been developed to overcome these problems in PBAs electrodes.[2,11,22,24] For instance, to alleviate Jahn-Teller distortion in certain PBAs, material modification strategies such as vacancy engineering[11] and substitution engineering[2] have been employed to remove or replace high-spin outer ions. The creation of vacancies by removing high-spin outer ions can

10.1002/anie.202414479

RESEARCH ARTICLE

inhibit the undesirable movement of coordination bonds, thereby minimizing Jahn-Teller distortion. Additionally, substituting atoms that cause strong Jahn-Teller distortion can help mitigate structural deterioration. Furthermore, lattice damage in certain PBAs can be prevented by using additives in the electrolyte through an electrolyte regulation method. This relies on the principle of common ion effect by which the added electrolyte breaks the precipitation/dissolution equilibrium of high-spin outer ions in PBAs and safeguards the lattice structure, thereby improving the cycling performance. However, the above two commonly employed methods proved to be insufficient to improve the cycling performance.[2,11] To prevent structural degradation to achieve the long cycle stability for the applications in aqueous electrolytes remains highly challenging.[22,24]

In this work, we report a novel strategy to stabilize the structure of $KCo[Fe(CN)_6]$ (labelled as KCoFe) by co-inserting Zn^{2+} and Co^{2+} ions into the KCoFe lattice, which induces a spontaneous and highly reversible phase conversion through the substitution of low-spin inner ions by additive metal ions from the electrolyte. The mechanism of the structural damage of KCoFe was studied by molecular orbital theory and crystal field theory, indicating the dissolution of high-spin outer ions and Jahn-Teller distortion as the predominant causes for the structural deterioration and capacity decay of KCoFe. The common ion effect by the addition of Co^{2+} ions in the Zn^{2+} electrolyte is first found as an effective strategy to suppress the dissolution of Co^{2+} from KCoFe. Co^{2+} and Zn^{2+} are simultaneously inserted into KCoFe lattices. Importantly, for the first time a co-insertion-induced spontaneous and reversible phase conversion from the single-phase (KCoFe) to bi-phasic ($K_2Co[Fe(CN)_6]$-$Zn_3[Co(CN)_6]_2$ system (denoted as K_2CoFe and ZnCo, respectively) upon discharging and then back to single-phase (KCoFe) based on the replacement of low-spin inner ion (Fe^{3+}) in KCoFe upon charging was detected. The coexistence of two phases was found to significantly relieve the Jahn-Teller distortion. As a result, in Zn^{2+}/Co^{2+} mixed electrolyte, KCoFe exhibited outstanding Zn^{2+} storage performance and excellent rate performance than that in pure Zn^{2+} electrolyte. A long-term cycling performance of over 4400 cycles at 40 C with the capacity retention of 97.7% was achieved. Lastly, the storage and migration mechanisms of dual ions in KCoFe have been investigated in depth using density functional theory calculations (DFT). This study opens up a new perspective for enhancing the electrochemical performance of PBAs for their practical applications of PBAs in aqueous energy storage systems.

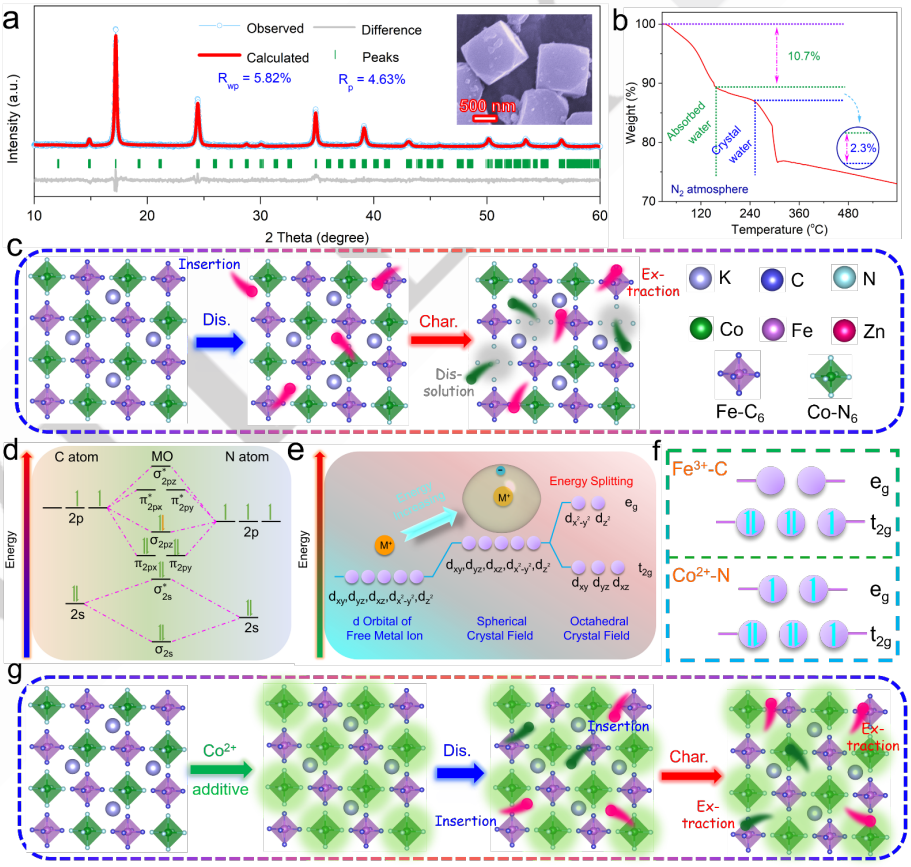

Figure 1. Theoretical analysis and schematic representations of structural damage for KCoFe. a Rietveld refinement XRD pattern of KCoFe. The insert is the SEM image of KCoFe. b TGA curve from room temperature to 600 °C in N_2 atmosphere. c Schematic representation of Co^{2+} dissolution process during electrochemical reaction. d The molecular orbital formula of -CN- group. e The energy level splitting of transition metal ion in octahedral field. f The d-orbital electron configuration of Fe^{3+}-C and Co^{2+}-N in KCoFe. g Schematic representation of the electrochemical process in Co^{2+} contained electrolyte.

10.1002/anie.202414479

Results and Discussion

Materials Characterization and Molecular Orbital/Crystal Field Theory Analysis

KCoFe, as a representative of PBAs, was synthesized by co-precipitation method at room temperature. Rietveld-refined X-ray diffraction (XRD) was applied to identify the crystallographic information of the as-prepared KCoFe. The crystal structure with high crystallinity is well matched with the space group of P1 (a = b = c = 10.2606 Å), as indicated in Figure 1a. The scanning electron microscopy (SEM) images showed uniformly distributed cubes of KCoFe with size about 1 μm (Inset in Figure 1a and Figure S1). Transmission electron microscopy (TEM) images (Figure S2) further demonstrated the cubic morphology and also revealed a characteristic d-spacing of 0.59 nm corresponding to the (111) plane. In addition, the selected area electron diffraction (SAED) patterns confirmed the polycrystalline features of KCoFe. The Energy Dispersive Spectroscopy (EDS) elemental mapping illustrated that the C, N, K, Co and Fe elements were uniformly distributed in KCoFe. Based on the elemental analysis results by inductively coupled plasma-optical emission spectroscopy (ICP-OES) (Table S1) and the determination of crystal water content by thermogravimetric analysis (TGA) of the weight loss between 155 and 250 °C (Figure 1b), the stoichiometric formula of KCoFe was determined to be $K_{0.89}Co[Fe(CN)_6]_{0.94}\cdot 0.38H_2O$. As shown in Figure S3, the characteristic stretching peak of -CN- group at 2088 cm^{-1} was clearly observed in Fourier transform infrared (FTIR) spectrum. The chemical valence states in KCoFe were analyzed by X-ray photoelectron spectroscopy (XPS, Figure S4), showing the co-existence of Fe^{3+}, Co^{2+} and Co^{3+}. The well defined structure of KCoFe with good crystallinity indicates its potential as an efficient electrode material.

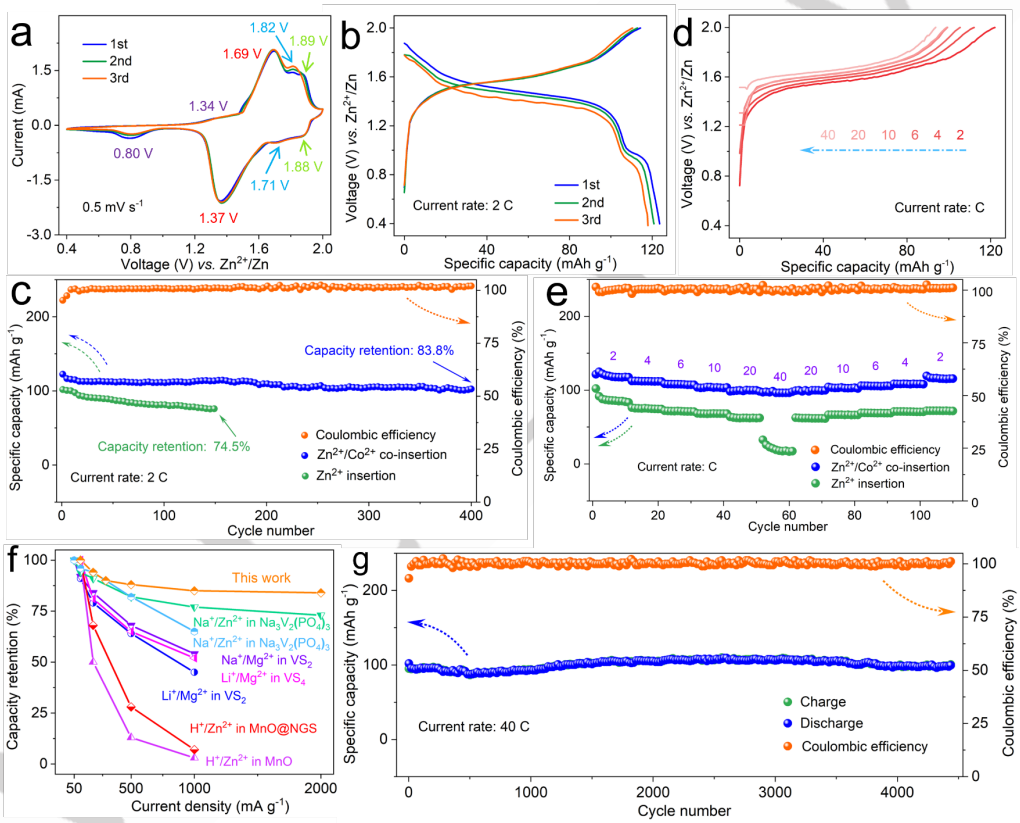

Figure 2. Electrochemical behavior of KCoFe electrode. a Typical CV curves at 0.5 mV s^{-1}. b The charge-discharge curves at 2 C. c The cycling performance of KCoFe electrode at 2 C in different electrolytes. d The charge curves of KCoFe electrode at different current rates. e The rate performance of KCoFe electrode in different electrolytes. f Comparison of rate performance between KCoFe electrode with other co-insertion materials. g Long-term cycling performance of KCoFe electrode at 40 C.

Despite its favorable properties, when used as electrode material for Zn^{2+} storage, pristine KCoFe shows unsatisfactory cycling performance. The main reason is the structural damage since the Co^{2+} ions in KCoFe dissolve from the framework (Table S2 and Figure S5). The dissolution process of Co^{2+} during the electrochemical reaction is displayed in Figure 1c. During the discharging process, Zn^{2+} ions insert into KCoFe. However, the Co^{2+} ions dissolve from the framework of KCoFe with the extraction of Zn^{2+} ions during charging process, resulting in severe lattice damage of KCoFe and thus poor cycling performance. To provide more insight on the poor cycling performance, the structural deterioration of KCoFe was for the first time theoretically studied by molecular orbital theory and crystal field theory. Molecular orbital theory can explain the electron filling in metal ions when they coordinate with ligands from the perspective of molecular orbitals. Crystal field theory

10.1002/anie.202414479

provides insight into the d-orbital energy level splitting in transition metal coordination compounds. In KCoFe, Fe and Co atoms are both octahedrally coordinated with six C and N atoms, respectively (Figure S6). Figure 1d shows the molecular orbital diagram of -CN- group in KCoFe, which is an electron pair donor. In contrast, the metal ion in the inner group is an electron pair acceptor, as depicted in Figure 1e by the energy level splitting of transition metal ion in octahedral field. In the free metal ion, the five d-orbitals are degenerate and therefore have the same energy.[25] In a spherical symmetric field, the energy of d-orbitals increases all together in the same way due to electrostatic repulsion, without d-orbital splitting. Finally, in a real octahedral field, the reduction in symmetry compared with a spherical field causes the splitting of the d orbitals into two energy groups: the higher-energy e_g orbitals and the lower-energy t_{2g} orbitals. This splitting arises due to the differing degrees of repulsive interaction between the d orbitals and the surrounding ligands.

Figure 1f displays the d-orbital electron configuration in KCoFe when transition metal ions are coordinated with different atoms. As -CN- group induces a strong field, Fe^{3+} with five valence electrons forms low-spin coordination with C atoms, and all five electrons are located in the low energy t_{2g} orbitals while the high energy e_g orbitals remain empty. Therefore, the Jahn-Teller distortion in this configuration is negligible, resulting in a stable system. However, when Co^{2+}, with seven valence electrons, is coordinated with N atoms, two electrons occupy the high-energy e_g orbitals, leading to high-spin coordination and a pronounced Jahn-Teller distortion. This distortion causes structural instability and poor cycling performance. Above theoretical studies by molecular orbital theory and the crystal field theory allow us a better understanding on the poor cycling performance of Prussian blue analogues as electrode materials. Currently, the most effective method to enhance the cycling performance of PBAs is based on the common ion effect by which the dissolution of high-spin outer ions is suppressed by adding the same ions into the electrolyte as additive.[22] As shown in Figure 1g, in an electrolyte containing Co^{2+} ions, the addition of Co^{2+} ions leads to a substantial increase in their concentration around the Co^{2+} ions within the KCoFe framework, thereby resulting in a common ion effect. During the discharging process, the additive Co^{2+} ions co-insert into the KCoFe together with the Zn^{2+} ions. During the charging process, only the inserted Co^{2+} and Zn^{2+} ions are extracted. Due to the common ion effect, the dissolution of Co^{2+} ions in the framework of KCoFe is efficiently suppressed, leading to improved cycling performance. Unfortunately, this improvement is still far from the exception in cycling performance, nevertheless, this gives a good guidance for the further improvement.

Electrochemical Behaviour of $KCo[Fe(CN)_6]$

The electrochemical behavior of KCoFe cathode was evaluated in aqueous Zn ion battery with zinc foil as anode and 3 M $ZnSO_4$ + 0.1 M $CoSO_4$ as electrolyte in comparison with that in pristine 3 M $ZnSO_4$ electrolyte without $CoSO_4$. KCoFe/Zn battery displayed four pairs of redox peaks at 1.89/1.88, 1.82/1.71, 1.69/1.37 and 1.34/0.80 V in the typical cyclic voltammetry (CV) curves in 3 M $ZnSO_4$ + 0.1 M $CoSO_4$ electrolyte (Figure 2a), which shows more redox peaks than those in pure 3 M $ZnSO_4$ electrolyte due to the co-insertion of Zn^{2+} and Co^{2+} ions (Figure S7). The first two pairs of peaks at 1.89/1.88 and 1.82/1.71 V can be attributed to the redox reaction of low-spin Fe^{3+}/Fe^{2+} couple coordinated with C atom in -CN-, while the other two at 1.69/1.37 and 1.34/0.80 V can be assigned to the high-spin Co^{3+}/Co^{2+} couple coordinated with N atom in -CN-. The presence of double peaks from a single redox species is most likely due to the insertion of Zn^{2+} into different lattice sites with different energies. The galvanostatic charge-discharge (GCD) curves that are indicative of the redox behavior (Figure 2b) further revealed that the charge/discharge capacities of the battery are 114.3/123.6 mAh g^{-1}, corresponding to a Coulombic efficiency of 92.5%. The excellent agreement between CV and GCD curves demonstrates the favorable reaction reversibility, which produces superior cycling performance (Figure 2c and Figure S8). After 400 cycles at 2 C, a high capacity retention of 83.8% was observed in $ZnSO_4/CoSO_4$ mixed electrolyte, corresponding to an extreme low capacity decay of 0.0405% per cycle. After 400 cycles, the main discharge platform can still remain flat and the XRD of the KCoFe electrode remains consistent with the initial one, indicating the excellent structural stability of KCoFe (Figure S9). In contrast, a lower capacity retention of 74.5% after 150 cycles with a capacity decay of as high as 0.17% per cycle was observed in pure $ZnSO_4$ electrolyte (Figure 2c).

Importantly, the rate performance of KCoFe (Figure 2d-e) was found to be highly improved in the presence of 3 M $ZnSO_4$ + 0.1 M $CoSO_4$ electrolyte. High specific capacities of 119.3, 112.4, 109.0, 103.8, 100.4, and 96.5 mAh g^{-1} were achieved at progressively increasing current rates of 2, 4, 6, 10, 20, and 40 C, respectively. Furthermore, the reaction demonstrated excellent reversibility, remaining highly stable even at ultra-high current rates, as indicated by the near 100% Coulombic efficiency observed at 40 C. In addition, the rate performance of the battery is much superior to other host materials reported in literatures (Figure 2f).[26-30] However, in pure 3 M $ZnSO_4$ electrolyte, KCoFe showed poor rate performance especially at a high current rate of 40 C. A low specific capacity of 19.8 mAh g^{-1} was recorded, being much lower than that measured in the case of 3 M $ZnSO_4$ + 0.1 M $CoSO_4$ electrolyte. It is important to note that KCoFe electrode showed impressive long-term cycling performance even at a high current rate of 40 C. Its specific capacity was retained at 99.7 mAh g^{-1} after over 4400 cycles (Figure 2g), corresponding to high capacity retention of 97.7%, being far superior to the cycling performance in pure 3 M $ZnSO_4$ electrolyte (Figure S10). Besides, KCoFe exhibited lower charge transfer resistance in 3 M $ZnSO_4$ + 0.1 M $CoSO_4$ electrolyte (0.9 Ω) than that in pure 3 M $ZnSO_4$ electrolyte (1.5 Ω), which is an important reason for the improvement in rate performance (Figure S11). The SEM images after 20 cycles showed that KCoFe can maintain a stable cubic structure in both electrolytes without structural damage (Figure S12).

It can be deduced from the above that the Zn^{2+} storage performance in KCoFe was significantly improved due to the presence of Co^{2+} in Zn^{2+} electrolyte. The common justification for this is that the addition of Co^{2+} ions effectively inhibited the dissolution of Co^{2+} from the KCoFe lattice due to the common ion

10.1002/anie.202414479

effect. However, the mere inhibition of the Co^{2+} dissolution from the KCoFe lattice cannot give such impressive long-term cycling performance. Hence the probability of Co^{2+}/Zn^{2+} co-insertion and its influence in improving cycling performance was further studied.

Spontaneous and Reversible Phase Conversion of $KCo[Fe(CN)_6]$

In order to explore the structural changes of KCoFe in different electrolytes, we compared the XRD patterns of KCoFe after discharging in different electrolytes. After discharging, the diffraction peaks of KCoFe are obviously asymmetric in pure 3 M $ZnSO_4$ electrolyte while KCoFe shows completely symmetrical diffraction peaks in 3 M $ZnSO_4$ + 0.1 M $CoSO_4$ electrolyte, indicating the Jahn-Teller distortion in KCoFe in pure 3 M $ZnSO_4$ electrolyte while this distortion is suppressed in 3 M $ZnSO_4$ + 0.1 M $CoSO_4$ electrolyte (Figure S13). In addition, the Rietveld refinements results showed that the diffraction angle and bond length of KCoFe in pure 3 M $ZnSO_4$ electrolyte are more obviously distorted than those in 3 M $ZnSO_4$ + 0.1 M $CoSO_4$ electrolyte, indicating that the severe Jahn-Teller distortion of KCoFe in pure 3 M $ZnSO_4$ electrolyte and the significant alleviation of lattice distortion in the mixed electrolyte. We also compared the XRD patterns of KCoFe at different charge states and verified that no by-products ($Zn_4(OH)_6SO_4$) were generated after the discharging process (Figure S14).

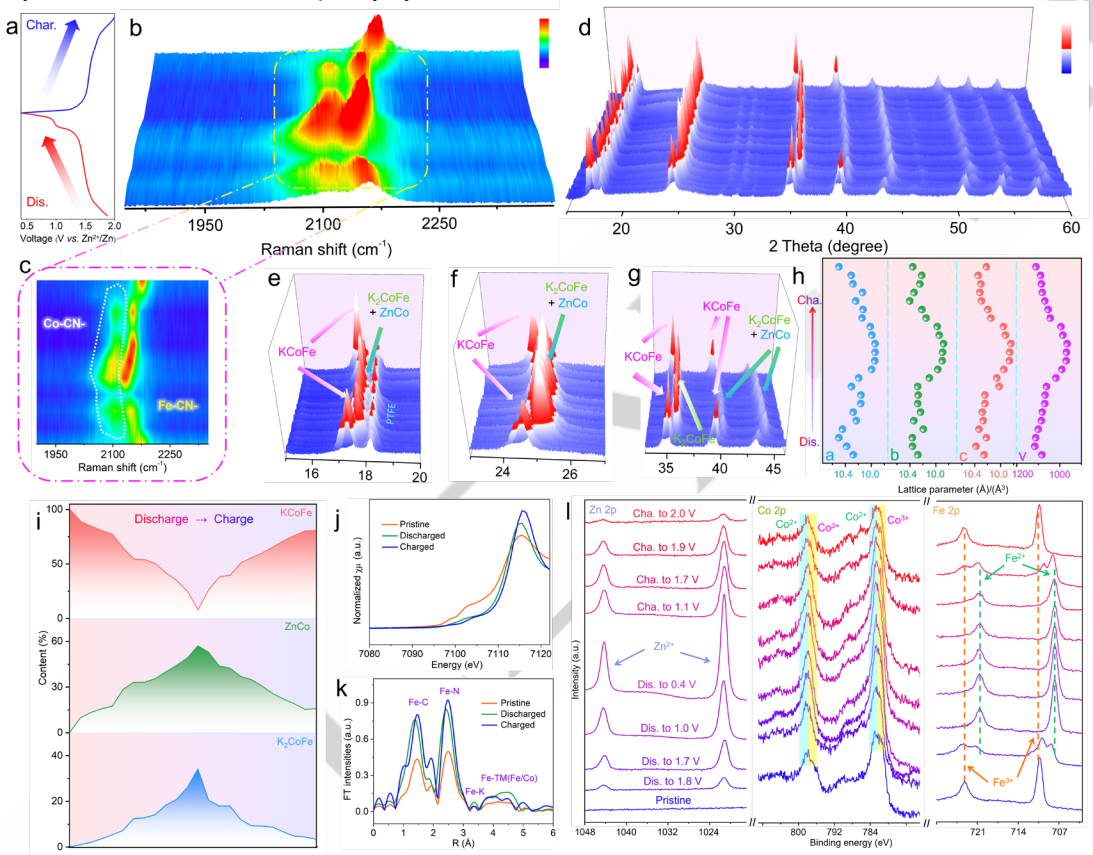

Figure 3. Investigation of the structural evolution and phase conversion of KCoFe electrode. a Charge-discharge curve. b Raman patterns of KCoFe electrode during the charge-discharge process. c Enlarged Raman regions of 1900-2350 cm^{-1}. d Overall XRD patterns of KCoFe electrode during the charge-discharge process. e-g Enlarged XRD regions of 15-20°, 23-27° and 33-46°. h Changes of lattice parameter a, b, c and unit cell volume (V). i Changes of phases content for KCoFe, ZnCo and K_2CoFe during charge-discharge process. g Ex-situ XANES of Fe K-edge of KCoFe electrodes at different states of charge. h The corresponding Fourier transformed EXAFS spectra. i Ex-situ XPS spectra for Zn 2p, Co 2p and Fe 2p at different states of charge.

The structural variation of KCoFe during discharging/charging process was monitored by Raman spectra and the corresponding charge-discharge curve was displayed in Figure 3a. During discharging process, the strong Raman peak at 2171 cm^{-1} corresponding to Fe-CN- gradually red-shifted to 2137 cm^{-1}, indicating the reduction reaction of Fe species in KCoFe.[31,32] After the charging process, the Raman peaks returned to the original positions, suggesting a reversible transformation of chemical valence and binding. More importantly, during the discharging process, a new peak at 2097 cm^{-1} was observed, corresponding to Co-CN- bond, indicating the formation of a new phase containing Zn and Co due to the co-insertion of Co^{2+} and Zn^{2+} (Figure 3b-c). After fully discharging, these two phases (Fe-CN- and Co-CN-) coexisted in the system, which is evidenced by their strong Raman peaks (Figure 3b-c and Figure S15). Moreover, the Raman peak of Co-CN- exhibited the same trend in shift as that of Fe-CN- and disappeared after fully charging, indicating the end of the phase conversion process (Figure 3c).

The crystalline phase evolution of KCoFe electrode during the electrochemical process was studied by XRD measurements, which reveals a phase conversion occurred between

10.1002/anie.202414479

RESEARCH ARTICLE

$KCo[Fe(CN)_6]$ and $K_2Co[Fe(CN)_6]/Zn_3[Co(CN)_6]_2$ ($K_2CoFe/ZnCo$) (Figure 3d and Figure S16). This indicates that KCoFe was converted to the two crystalline phases of K_2CoFe and ZnCo upon Zn^{2+} and Co^{2+} co-insertion. As depicted in Figure 3e-g and Figure S17, the phase conversion was reflected in the changes in the relative intensity and Bragg position of the featured diffraction peaks. On the one hand, the peaks at 17.4° and 39.3°, originally attributed to KCoFe, were significantly weakened and shifted to 17.7° and 40.1°, corresponding to the formation of K_2CoFe and ZnCo phases. Additionally, new peaks at 25.1° and 44.0°, both associated with K_2CoFe and ZnCo, were notably intensified. A diffraction peak at 35.7°, corresponding to K_2CoFe, was also detected, with its relative intensity significantly enhanced during the phase conversion from KCoFe to K_2CoFe. Upon the extraction of Zn^{2+} and Co^{2+} after the charging process, the K_2CoFe and ZnCo phases were retransformed into KCoFe, and the relative intensities and Bragg positions of all diffraction peaks were restored to those of the original KCoFe electrode, indicating the excellent reversibility of the phase conversion reaction and the structural stability of KCoFe. Therefore, a novel phase conversion reaction occurs when the low-spin inner ion (Fe^{3+}) in KCoFe is replaced because of the co-insertion of Zn^{2+} and Co^{2+}. Besides, the Jahn-Teller distortion is also relieved due to the appearance of a new conversion phase in the system. Therefore, the synergy between phase conversion process and common ion effect led to excellent Zn^{2+} ion storage capacity in KCoFe.

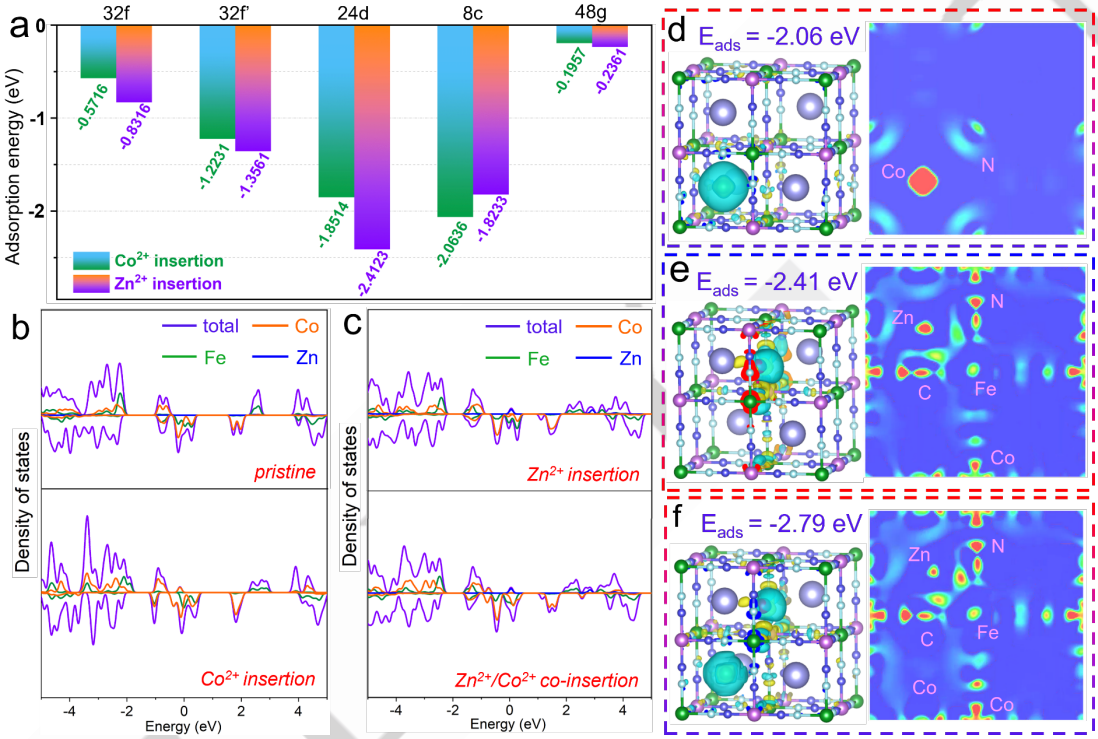

Figure 4. Density functional theory calculations on reaction mechanism. a The adsorption energies of Zn^{2+} and Co^{2+} co-insertion into different sites. b, c Density of states for KCoFe electrode at different ions inserted states. d-f Differential charge density for KCoFe electrode at different ions inserted states.

To further explore the structural changes of KCoFe during the charging and discharging process, we quantitatively studied the changes in lattice parameters and phase contents at different states of charge-discharge by Rietveld refinements (Figures S18-21). During the discharging process, the lattice parameters of a, b and c gradually decreased from 10.2783, 10.2755 and 10.2539 Å to 9.9407, 9.8788 and 9.8399 Å, respectively, and the corresponding unit cell volume decreased from 1082.94 to 968.99 $Å^3$, indicating the lattice contraction of the system (Figure 3h). After full charge, the lattice parameters of a, b and c recovered to 10.5004, 10.3662 and 10.2134 Å, respectively, and the corresponding unit cell volume was 1110.76 $Å^3$, indicating the lattice expansion of the system. In addition, the discharging process was accompanied by the decrease of the content of KCoFe phase and an increase in the content of ZnCo and K_2CoFe phases. At the fully discharged state, the contents of KCoFe, ZnCo and K_2CoFe phases are 7.85%, 57.1% and 34.1% (Figure 3i), respectively, which proves that the co-insertion of Zn^{2+} and Co^{2+} leads to the formation of two new phases in the system. After fully charged, the contents of KCoFe, ZnCo and K_2CoFe phases are 80.7%, 15.8% and 3.5%, respectively. Therefore, the reversible changes in unit cell parameters and phase contents indicate the reversibility of the electrochemical reaction of the system.

The changes in chemical bond in KCoFe during the electrochemical reaction were monitored by X-ray absorption near-edge spectroscopy (XANES), XPS and FTIR characterization techniques. Figure 3j shows the normalized XANES spectra of the Fe K-edge at different states of charge-discharge. The detectable pre-edge peak at 7098 eV indicates a symmetric octahedral coordination environment around the Fe atom.[33,34] The strong covalent bonds between Fe atom and -CN- ligand were stable throughout the electrochemical process, which was proved by the shoulder peak at 7105 eV.[34]

10.1002/anie.202414479

RESEARCH ARTICLE

Importantly, the main Fe K-edge peak slightly shifted to lower energy position (7115 eV) after discharging process and returned to the pristine energy position (7116 eV) after charging process, which clearly indicated the reversible change in Fe valence from Fe^{3+} to Fe^{2+} and then back to Fe^{3+} state.[6,35] Therefore, both the structural stability and reversible valence evolution of KCoFe electrode were verified by the XANES spectra. In addition, Fourier transformed (FT) extended X-ray absorption fine structure (EXAFS) spectroscopy was performed to further analyze the change in bond distance around central Fe atom. As displayed in Figure 3k, four distinct regions at 1.5, 2.5, 3.4 and 3.6-4.9 Å were observed, which can be assigned to Fe-C, Fe-N, Fe-K and Fe-TM (Fe/Co) bonds, respectively.[25,36] The Fe-C and Fe-N bond distances were found to decrease after the discharge process, indicating the reduction of Fe^{3+} to Fe^{2+}. The subsequent increase in Fe-C and Fe-N bond distances observed after the charging process demonstrates the reversible structural contraction and expansion of KCoFe during the insertion and extraction of both Zn^{2+} and Co^{2+} ions.

The changes in the chemical states and elemental contents of Zn, Co and Fe in KCoFe were investigated using XPS spectroscopy (Figure 3l). Since the Fe content remains constant during different states of charge, we used Fe as the reference to check the content of Zn and Co elements. As shown in Figure S22, the Zn/Fe ratio dramatically increased to 0.67 after discharging process and then gradually decreased to 0.23 after charging process, indicating the reversible insertion and extraction of Zn^{2+}. Furthermore, the presence of mixed valence of Co^{2+} and Co^{3+} in pristine KCoFe was clearly observed. The Co/Fe ratio increased to 0.86 from 0.55 after discharging process. The increase in the content of Co specie and Co^{2+} upon discharging can be attributed to both the insertion of Co^{2+} and the partial reduction of Co^{3+} to Co^{2+} in KCoFe. After charging process, The Co/Fe ratio decreased to 0.57, which confirmed the reversible extraction of Co^{2+}. The Co/Fe and Zn/Fe ratios at different states of charge-discharge can also be calculated from the ICP results in Figure S23. The Co/Fe ratio increases to 0.77 from 0.52 after discharging and then returns to 0.57 after charging. The Zn/Fe ratios of 0.78 and 0.21 at full discharge and charge also confirms the insertion and extraction of Zn^{2+}. In addition, different from the partial redox reaction of Co species, Fe^{3+} was completely reduced to Fe^{2+} after Zn^{2+} and Co^{2+} co-insertion. All Fe^{2+} were oxidized to Fe^{3+} after charging process, which indicated that Fe species had stronger electrochemical reactivity than Co species. This result was found to be in good agreement with CV test. The results from XPS analysis not only revealed the reversible valence variations in KCoFe, but also proved the reaction characteristics of different elements, which are related to their electrochemical behaviors.

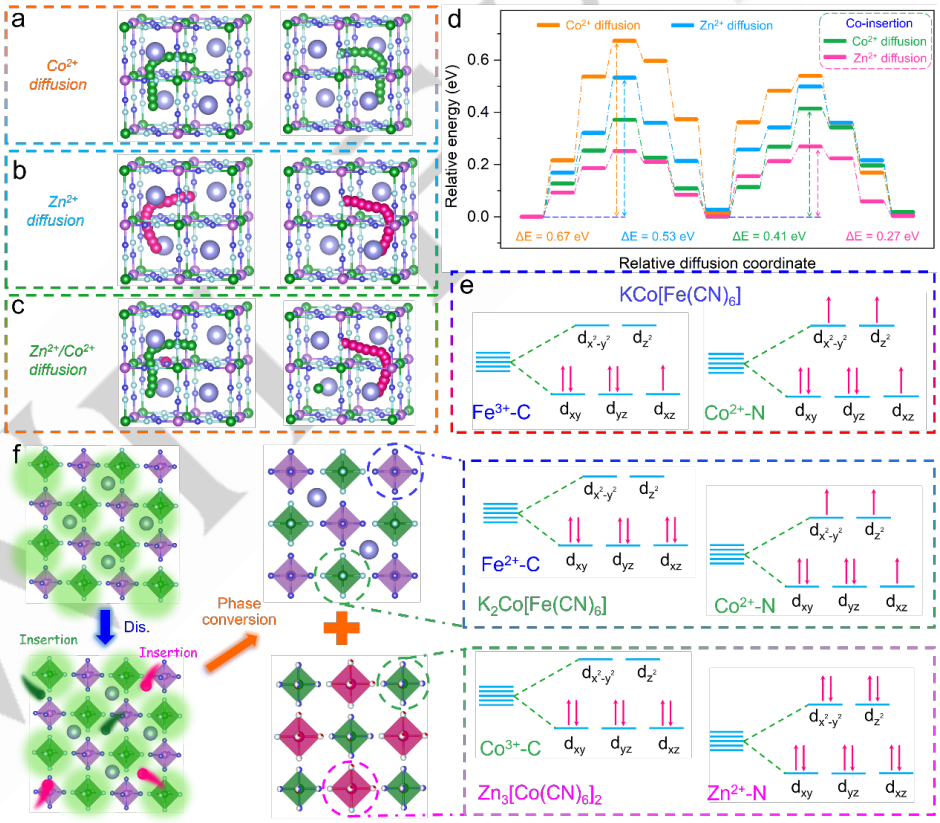

Figure 5. Density functional theory calculations on diffusion mechanism. a-c The diffusion pathways of Co^{2+}, Zn^{2+} and Zn^{2+}/Co^{2+} in KCoFe. d The corresponding diffusion energy barrier profiles. e The electron filling diagram of Fe^{3+}-C and Co^{2+}-N in KCoFe. f Phase conversion process and the electron filling diagram of Fe^{2+}-C and Co^{2+}-N in K_2CoFe and Co^{3+}-C and Zn^{2+}-N in ZnCo.

The reversible structural evolution of KCoFe proved by XANES and XPS measurements upon cycle was further verified through FTIR spectroscopy (Figure S24). A slight red shift and blue shift of cyano-group were detected during the discharging

and charging process respectively. In addition, the SEM images show that after 50, 200 and 400 cycles, the complete cubic morphology of KCoFe and the average distribution of different elements can be maintained (Figure S25), indicating the structural stability of KCoFe. All the above results confirmed that a spontaneous and high reversible phase conversion between a single phase of $KCo[Fe(CN)_6]$ and the co-existence of $K_2Co[(CN)_6]/Zn_3[Co(CN)_6]_2$ upon discharging and charging in electrolyte containing Zn^{2+} and Co^{2+}.

DFT Calculations

To further explore the conversion reaction mechanism, density functional theory (DFT) calculations were performed. The possibility of Zn^{2+} and Co^{2+} co-insertion into KCoFe was verified by calculating their energies when inserted in different sites. As shown in Figure 4a and Figures S26-27, KCoFe exhibited abundant interstitial sites for ion storage, such as the Wyckoff positions of 8c, 24d, 32f, 32f' and 48g.[37] The insertion energies of Zn^{2+} and Co^{2+} at all sites were negative, indicating that both Zn^{2+} and Co^{2+} can theoretically be inserted into these sites. The lowest energy upon Zn^{2+} insertion is -2.41 eV, indicating that the optimal insertion site for Zn^{2+} is 24d site, while for Co^{2+} it was -2.06 eV, indicating that it was more inclined to insert at the 8c site. The density of states (DOS) was used to account for the changes in the electronic structure of KCoFe after Zn^{2+} and Co^{2+} insertion (Figure 4b-c). The calculated results indicate that the system showed favorable electronic conductivity because the DOS values near the Fermi level were not zero. When Zn^{2+} and Co^{2+} were co-inserted, the DOS peak was weakened, indicating that the degeneracy of the system was reduced. This suggests that the co-insertion of Zn^{2+} and Co^{2+} ions alleviates the Jahn-Teller distortion in the system, resulting in increased stability. In addition, the change of DOS on Fe was found to be stronger than that on Co, indicating that Fe species had a higher redox activity,[37] which is consistent with the results from XPS.

To study the charge transfer in the system upon Zn^{2+} and Co^{2+} co-insertion, differential charge density calculations were performed. As shown in Figure 4d-f, the co-insertion of Zn^{2+} and Co^{2+} resulted in the lowest energy of -2.79 eV compared with the insertion of Zn^{2+} or Co^{2+} alone, indicating enhanced system stability. In contrast, the insertion of Co^{2+} alone did not produce a significant change in the charge density of the system. While Zn^{2+} was inserted, the accumulation of charges around Zn^{2+} became evident, indicating the formation of chemical bonds.[38,39] More importantly, when Zn^{2+} and Co^{2+} were co-inserted, not only the apparent charge accumulation around Zn^{2+} became more pronounced, but also a small amount of charge accumulation around Co^{2+} appeared, indicating the formation of stronger chemical bonds. These studies confirmed that the co-insertion of Zn^{2+} and Co^{2+} played an important role in stabilizing the system and in forming Co-CN chemical bonds.

In addition, diffusion behavior of ions was studied by DFT calculations. Figure 5a-c and Figures S28-30 illustrate the diffusion pathways of Zn^{2+}, Co^{2+}, and Zn^{2+}/Co^{2+} in KCoFe from various perspectives. It was observed that both Zn^{2+} and Co^{2+} diffuse from their inserted sites in KCoFe along optimal diffusion pathways, although they follow different migration routes. Impressively, when Zn^{2+} and Co^{2+} were co-inserted, their respective diffusion was not adversely affected by each other, which can be proved by similar migration pathways. The corresponding diffusion energy barriers are depicted in Figure 5d. Compared with only Zn^{2+} or only Co^{2+} insertion alone (0.53 eV for Zn^{2+} and 0.67 eV for Co^{2+}), Zn^{2+}/Co^{2+} co-insertion showed lower diffusion energy barrier (0.27 eV for Zn^{2+} and 0.41 eV for Co^{2+}), which indicates that co-insertion accelerated ion transport and enabled excellent rate performance. The possible reasons are the coexistence of two-phases and minimized Jahn-Teller distortion caused by the co-insertion of Zn^{2+} and Co^{2+}. Figure 5e shows the molecular orbital formulae of Fe^{3+}-C and Co^{2+}-N in pristine KCoFe, while Figure 5f shows the molecular orbital formulae of Fe^{2+}-C, Co^{2+}-N, Zn^{2+}-N and Co^{3+}-C in discharged products of K_2CoFe and ZnCo (Figure S31). It was observed that Fe^{2+}-C in K_2CoFe exhibited weak Jahn-Teller distortion, as all electrons were filled in the low-energy t_{2g} orbital. In contrast, Co^{2+}-N showed strong Jahn-Teller distortion, leading to a distortion of the structure. The transformation of KCoFe phase into ZnCo and K_2CoFe reduced the content of K_2CoFe in the discharged products, thereby minimizing the Jahn-Teller distortion of Co^{2+}-N. Compared with Fe^{2+}-C and Co^{2+}-N, the electron configurations of Zn^{2+}-N and Co^{3+}-C in ZnCo were highly symmetrical, resulting in no Jahn-Teller distortion and thereby enhancing structural stability. Consequently, KCoFe demonstrated high structural reversibility, contributing to its excellent long-term cycling stability and rate performance for Zn^{2+} storage.

Conclusion

In this work, we report a spontaneous and reversible phase conversion phenomenon in $KCo[(CN)_6]$ induced by co-insertion of carrier ion (Zn^{2+}) and additive ion (Co^{2+}) in electrolyte, which plays an important role in improving the electrochemical performance of KCoFe. On the one hand, the presence of additive Co^{2+} in the electrolyte effectively inhibits the dissolution of Co^{2+} from KCoFe and ensures the structural stability. On the other hand, due to the co-insertion of Co^{2+} and Zn^{2+} into KCoFe, two new phases of K_2CoFe and ZnCo were generated in the system. More importantly, this phase conversion is quite different from previously reported substitution of high-spin outer ions in PBAs, but as it is caused by the substitution of low-spin inner ion (Fe^{3+}) in KCoFe. The generation of the new phase can effectively alleviate the Jahn-Teller distortion of the system and avoid the damage of the structure. As a result, by incorporating Co^{2+} in Zn^{2+}, KCoFe exhibits superior electrochemical performance in Co^{2+} containing electrolyte compared with pure Zn^{2+} electrolyte. At a high current rate of 40 C, the capacity retention rate is as high as 80.9%, which reflects excellent rate performance. Moreover, KCoFe also exhibits ultra-long cycling performance over 4400 cycles. Therefore, the co-insertion-induced spontaneous phase replacement reaction provides a novel perspective for further exploring the storage mechanism of PBAs in rechargeable batteries.

Supporting Information

Experimental details, list of used chemicals, materials synthesis, materials characterization, electrochemical measurements, computational methods and additional data for SEM, TEM, FTIR, XPS, electrochemical performance, Raman, XRD, ICP.

The authors have cited additional references within the Supporting Information.[40-45]

Acknowledgements

This work is supported by National Natural Science Foundation of China (U2330205, U1830106, U1663225), National Key R&D Program of China (2021YFE0115800), the 111 National Project (B20002) from Ministry of Science and Technology and Ministry of Education of China, Ningbo Natural Science Foundation (2022J064) and Wallonia Government in the frmae of “Plan de Relance” (2310153-BatFactory).

Keywords: Prussian blue analogues • Aqueous zinc ion battery • Structural damage• common ion effect • Phase conversion

References:

[1] W. Wang, Y. Gang, Z. Hu, Z. Yan, W. Li, Y. Li, Q. Gu, Z. Wang, S. Chou, H. Liu, S. Dou, *Nat. Commun.* **2020**, *11*, 980.

[2] J. Ge, L. Fan, A. Rao, J. Zhou, B. Lu, *Nat. Sustain.* **2022**, *5*, 225-234.

[3] C. Liu, X. Wang, W. Deng, C. Li, J. Chen, M. Xue, R. Li, F. Pan, *Angew. Chem. Int. Ed.* **2018**, *57*, 7046-7050.

[4] S.T. Senthilkumar, H. Bae, J. Han, Y. Kim, *Angew. Chem. Int. Ed.* **2018**, *57*, 5335-5339.

[5] L. Ma, X. Li, G. Zhang, Z. Huang, C. Han, H. Li, Z. Tang, C. Zhi, *Energy Storage Mater.* **2020**, *31*, 451-458.

[6] W. Deng, Z. Li, Y. Ye, Z. Zhou, Y. Li, M. Zhang, X. Yuan, J. Hu, W. Zhao, Z. Huang, C. Li, H. Chen, J. Zheng, R. Li, *Adv. Energy Mater.* **2021**, *11*, 2003639.

[7] L. Ma, H. Cui, S. Chen, X. Li, B. Dong, C. Zhi, *Nano Energy* **2021**, *81*, 105632.

[8] X. Zhang, M. Xia, H. Yu, J. Zhang, Z. Yang, L. Zhang, J. Shu, *Nano-Micro Lett.* **2021**, *13*, 139.

[9] X. Wu, J. Hong, W. Shin, L. Ma, T. Liu, X. Bi, Y. Yuan, Y. Qi, T. Surta, W. Huang, J. Neuefeind, T. Wu, P. Greaney, J. Lu, X. Ji, *Nature Energy* **2019**, *4*, 123-130.

[10] M. Xia, X. Zhang, H. Yu, Z. Yang, S. Chen, L. Zhang, M. Shui, Y. Xie, J. Shu, *Chem. Eng. J.* **2021**, *421*, 127759.

[11] Y. Shang, X. Li, J. Song, S. Huang, Z. Yang, Z. Xu, H. Yang, *Chem 2020*, *6*, 1804-1818.

[12] C. Xu, Z. Yang, X. Zhang, M. Xia, H. Yan, J. Li, H. Yu, L. Zhang, J. Shu, *Nano-Micro Lett.* **2021**, *13*, 166.

[13] Y. Zeng, X.F. Lu, S.L. Zhang, D. Luan, S. Li, X.W.(David) Lou, *Angew. Chem. Int. Ed.* **2021**, *60*, 22189-22194.

[14] Y. Zeng, J. Xu, Y. Wang, S. Li, D. Luan, X.W.(David) Lou, *Angew. Chem. Int. Ed.* **2022**, *61*, e202212031.

[15] M. Cui, Y. Zhu, H. Lei, A. Liu, F. Mo, K. Ouyang, S. Chen, X. Lin, Z. Chen, K. Li, Y. Jiao, C. Zhi, Y. Huang, *Angew. Chem. Int. Ed.* **2024**, *63*, e202405428.

[16] K. Hurlbutt, S. Wheeler, I. Capone, M. Pasta, *Joule* **2018**, *2*, 1950-1960.

[17] J. Qian, C. Wu, Y. Cao, Z. Ma, Y. Huang, X. Ai, H. Yang, *Adv. Energy Mater.* **2018**, *8*, 1702619.

[18] L. Jiang, Y. Lu, C. Zhao, L. Liu, J. Zhang, Q. Zhang, X. Shen, J. Zhao, X. Yu, H. Li, X. Huang, L. Chen, Y. Hu, *Nature Energy* **2019**, *4*, 495-503.

[19] J. Song, L. Wang, Y. Lu, J. Liu, B. Guo, P. Xiao, J. Lee, X. Yang, G. Henkelman, J. Goodenough, *J. Am. Chem. Soc.* **2015**, *137*, 2658-2664.

[20] F. Gebert, D. Cortie, J. Bouwer, W. Wang, Z. Yan, S. Dou, S. Chou, *Angew. Chem. Int. Ed.* **2021**, *60*, 18519-18526.

[21] B. Wang, Y. Han, X. Wang, N. Bahlawane, H. Pan, M. Yan, Y. Jiang, *iScience* **2018**, *3*, 110-133.

[22] X. Zhang, M. Xia, T. Liu, N. Peng, H. Yu, R. Zheng, L. Zhang, M. Shui, J. Shu, *Chem. Eng. J.* **2021**, *421*, 127767.

[23] M. Chen, Q. Liu, S. Wang, E. Wang, X. Guo, S. Chou, *Adv. Energy Mater.* **2019**, *9*, 1803609.

[24] L. Ma, S. Chen, H. Li, Z. Ruan, Z. Tang, Z. Liu, Z. Wang, Y. Huang, Z. Pei, J. Zapiena, C. Zhi, *Energy Environ. Sci.* **2018**, *11*, 2521.

[25] S. Guo, J. Li, B. Zhang, W. Chen, G. Fang, M. Long, S. Liang, *Sci. Bull.* **2022**, *67*, 626-635.

[26] X. Hu, J. Peng, F. Xu, M. Ding, *ACS Appl. Mater. Interfaces* **2021**, *13*, 57252-57263.

[27] W. Li, X. Gao, Z. Chen, R. Guo, G. Zou, H. Hou, W. Deng, X. Ji, J. Zhao, *Chem. Eng. J.* **2020**, *402*, 125509.

[28] Y. Wang, C. Wang, X. Yi, Y. Hu, L. Wang. L. Ma, G. Zhu, T. Chen, Z. Jin, *Energy Storage Mater.* **2019**, *23*, 741-748.

[29] P. Hu, T. Zhu, X. Wang, X. Zhou, Xi. Wei, X. Yao, W. Luo, C. Shi, K. Owusu, L. Zhou, L. Mai, *Nano Energy* **2019**, *58*, 492-498.

[30] Q. Li, K. Ma, C. Hong, G. Yang, C. Wang, *Sci. China Mater.* **2021**, *64*, 1386-1395.

[31] Y. Liu, D. He, Y. Cheng, L. Li, Z. Lu, R. Liang, Y. Fan, Y. Qiao, S. Chou, *Small* **2020**, *16*, 1906946.

[32] G. Du, M. Tao, J. Li, T. Yang, W. Gao, J. Deng, Y. Qi, S. Bao, M. Xu, *Adv. Energy Mater.* **2020**, *10*, 1903351.

[33] M. Giorgetti, L. Guadagnini, D. Tonelli, M. Minicuccib, G. Aquilantic, *Phys. Chem. Chem. Phys.* **2012**, *14*, 5527-5537.

[34] B. Xie, P. Zuo, L. Wang, J. Wang, H. Huo, M. He, J. Shu, H. Li, S. Lou, G. Yin, *Nano Energy* **2019**, *61*, 201-210.

[35] W. Li, C. Han, W. Wang, Q. Xia, S. Chou, Q. Gu, B. Johannessen, H. Liu, S. Dou, *Adv. Energy Mater.* **2020**, *10*, 1903006.

[36] Y. You, X. Yu, Y. Yin, K. Nam, Y. Guo, *Nano Res.* **2015**, *8*, 117-128.

[37] C. Ling, J. Chen, F. Mizuno, *J. Phys. Chem. C* **2013**, *117*, 21158-21165.

[38] S. Chen, Q. Chen, J. Ma, J. Wang, K. Hui, J. Zhang, *Small* **2022**, *18*, 2200168.

[39] S. Dong, W. Shin, H. Jiang, X. Wu, Z. Li, J. Holoubek, W. Stickle, B. Key, C. Liu, J. Lu, P. Greaney, X. Zhang, X. Ji, *Chem* **2019**, *5*, 1-15.

[40] G. Kresse, J. Furthmüller, *Phys. Rev. B* **1996**, *54*, 11169-11186.

[41] J. Perdew, K. Burke, M. Ernzerhof, *Phys. Rev. Lett.* **1996**, *77*, 3865-3868.

[42] G. Kresse, D. Joubert, *Phys. Rev. B* **1999**, *59*, 1758-1775.

[43] P. Blöchl, *Phys. Rev. B* **1994**, *50*, 17953-17979.

[44] S. Grimme, J. Antony, S. Ehrlich, K. Krieg, *J. Chem. Phys.* **2010**, *132*, 154104.

[45] G. Henkelman, B. Uberuaga, H. Jónsson, *J. Chem. Phys.* **2000**, *113*, 9901.

[46] Deposition numbers 1603712 (for **$K_2Co[Fe(CN)_6]$**), and 1635810 (for **$Zn_3[Co(CN)_6]_2$**) contain the supplementary crystallographic data for this paper. These data are provided free of charge by the joint Cambridge Crystallographic Data Centre and Fachinformationszentrum Karlsruhe Access Structures service. The crystallographic data can also be found

10.1002/anie.202414479

at the National Center for Biotechnology Information of America https://pubchem.ncbi.nlm.nih.gov/compound. PubChem CIDs 129675076 (for **KCo[Fe(CN)$_6$]**), 171039961 (for **K$_2$Co[Fe(CN)$_6$]**), and 129635807 (for **Zn$_3$[Co(CN)$_6$]$_2$**).

10.1002/anie.202414479

WILEY VCH

RESEARCH ARTICLE

Table of Contents Graphic

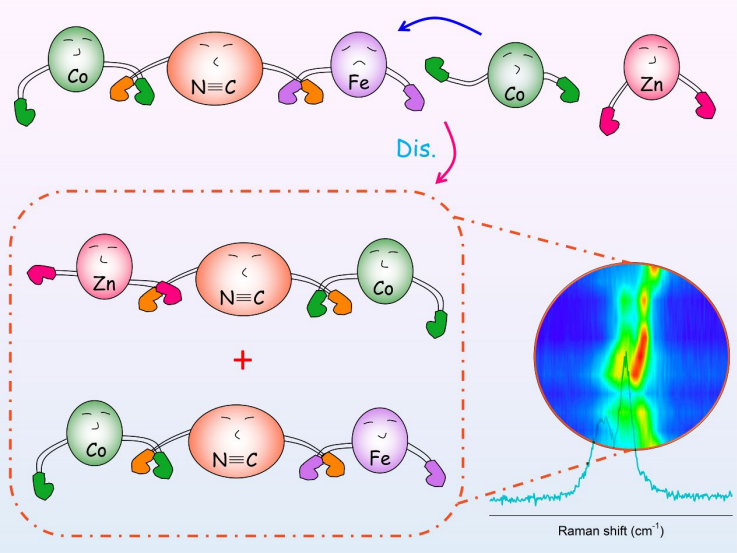

An innovative electrolyte regulation strategy is developed to improve the performance of $KCo[Fe(CN)_6]$ cathode in aqueous zinc ion battery. The dissolution of high-spin metal ion (Co) in $KCo[Fe(CN)_6]$ is suppressed. The dual ion co-insertion induces a novel and reversible phase conversion reaction in which low-spin atom (Fe) in $KCo[Fe(CN)_6]$ are replaced. An ultra-long life aqueous zinc ion battery is achieved.